Check for updates

Rational design direct Z-scheme BiOBr/g-C$_3$N$_4$ heterojunction with enhanced visible photocatalytic activity for organic pollutants elimination

Hongfei Li, Aiqiong Ma, [ID] * Dian Zhang, Yunqin Gao and Yonghao Dong

A rapid recombination of photo-generated electrons and holes, as well as a narrow visible light adsorption range are two intrinsic defects in graphitic carbon nitride (g-C$_3$N$_4$)-based photocatalysts. Inspired by natural photosynthesis, an artificially synthesized Z-scheme photocatalyst can efficaciously restrain the recombination of photogenerated electron−hole pairs and enhance the photoabsorption ability. Hence, to figure out the above problems, BiOBr/g-C$_3$N$_4$ composite photocatalysts with different mass ratios of BiOBr were successfully synthesized *via* a facile template-assisted hydrothermal method which enabled the BiOBr microspheres to *in situ* grow on the surface of g-C$_3$N$_4$ flakes. Furthermore, to explore the origin of the enhanced photocatalytic activity of BiOBr/g-C$_3$N$_4$ composites, the microstructure, photoabsorption ability and electrochemical property of BiOBr/g-C$_3$N$_4$ composites were investigated by X-ray diffraction (XRD), field emission scanning electron microscopy (FESEM), transmission electron microscopy (TEM), UV-vis diffuse reflectance spectroscopy (DRS), electrochemical impedance spectroscopy (EIS) and photocurrent (PC) response measurements. As a result, the introduction of BiOBr on g-C$_3$N$_4$ to constitute a direct Z-scheme heterojunction system can effectively broaden the light absorption range and promote the separation of photo-generated electron−hole pairs. Hence, compared with pure g-C$_3$N$_4$ and BiOBr, the resultant BiOBr/g-C$_3$N$_4$ composites exhibit the remarkable activity of photodegradated rhodamine B (RhB) and tetracycline hydrochloride (TC-HCl) under visible light irradiation. Simultaneously, the optimal BiOBr content of the BiOBr/g-C$_3$N$_4$ composites was obtained. The BiOBr/g-C$_3$N$_4$ composites exhibit an excellent photostability and reusability after four recycling runs for degradation RhB. Moreover, the active-group-trapping experiment confirmed that ·OH, ·O$_2^-$ and h$^+$ were the primary active groups in the degradation process. Based on the above research results, a rational direct Z-scheme heterojunction system is contrastively analyzed and proposed to account for the photocatalytic degradation process of BiOBr/g-C$_3$N$_4$ composites.

1. Introduction

With the development of dye and pharmaceuticals industry, organic pollutants of industrial emission have given rise to severe water pollution which could constitute a bad threat to the living environment of humanity. Thereinto, aromatic compounds with diffusely conjugated chromophores, such as RhB and TC-HCl, possess a physicochemical stability in water environment such that the traditional treatment measures hardly prove effective. Therefore, plenty of new technologies which can effectively decompose organic pollutants through redox reactions have emerged continuously.[1–3] Semiconductor photocatalytic degradation technology has attracted a wide research interest,[4,5] due to its unique advantages of the utilization visible light to excite semiconductor materials to produce highly efficient active groups.[6,7] Nevertheless, most semiconductor photocatalysts with a wide band gap can merely utilize the ultraviolet light approximately, which accounts for only 4% of the solar energy.[8,9] Although CdS,[10] BiVO$_4$,[11] Ag$_3$PO$_4$,[12] *etc.* with relatively narrow band gaps possess a visible light photocatalytic activity, they usually suffer from a rapid recombination between excited electrons and holes during light irradiation.[13] As a consequence, it is attractive and significant to design and develop photocatalytic materials with the applicable band gaps, wide visible-light adsorption ranges and highly photocatalytic activity.[14]

Graphitic carbon nitride (g-C$_3$N$_4$), a familiar metal-free semiconductor photocatalyst, has been frequently investigated because of its numerous excellent physicochemical traits, such as outstanding thermology, electricity and photology properties.[15] Such performances result mainly from its stratiform

College of Materials Science and Engineering, Xi'an University of Architecture and Technology, Xi'an, Shaanxi 710055, China. E-mail: maaiqiong@xauat.edu.cn

structure of strong covalent C–N bonds in each layer and weak van der Waals force between layers.[16,17] The g-C_3N_4 with a narrow band gap (2.7 eV) possesses an appropriate conduction band (CB) position ($E_{CB} = -1.07$ eV), which is more negative than the reduction potential of $E^0(O_2/\cdot O_2^-)$ (about -0.33 eV).[18] Therefore, the photo-generated electrons on the CB of g-C_3N_4 are capable of reacting with O_2 to generate superoxide radicals ($\cdot O_2^-$) which can subsequently participate in the process of degradation of organic pollutants. Nevertheless, on account of the weak van der Waals interactions between adjacent CN layers in the g-C_3N_4 crystal structure, g-C_3N_4 has high recombination odds of photo-generated electron–hole pairs which lessens the quantum efficiency of the photocatalytic degradation procedures.[19,20] Therefore, for further improving the inherent shortcomings of g-C_3N_4 and enhancing its photocatalytic efficiency, several research works have been carried out and showed that combination with metal-oxide semiconductors to construct composite photocatalyst can remarkably enhance the absorption ability of sunlight and prolong the lifetime of the photogenerated carrier.[21]

Recently, BiOBr, as one of the highly active bismuth oxyhalide (BiOX, X = Cl, Br, I) photocatalytic materials, has received intensive attention in the photocatalytic field. It exhibits a high photocatalytic activity on account of its suitable band gap (2.81 eV) and wide visible light adsorption range (>410 nm).[22] It is noteworthy that its unique lamellar crystal structure, just as the tetragonal matlockite structure, can afford adequate space to polarize the relevant atoms and orbitals, resulting in the generation of an internal electric field between the $[Bi_2O_2]^{2+}$ layer and the Br^- layer.[23] On the basis of previous reports, BiOBr was used to combine with g-C_3N_4 to form an indirect Z-scheme heterojunction and showed excellent photocatalytic activity. In 2019, Zhang Mingming *et al.* prepared an indirect Z-scheme BiOBr/CDs/g-C_3N_4 photocatalyst by a facile hydrothermal method and the hybrids can degrade 17.5% of tetracycline (TC) within 180 min for which the reaction rates were 31.92 and 9.76 times those of pristine BiOBr and g-C_3N_4, respectively.[24] Hence, this indirect Z-scheme-type composite shows remarkable potential as an efficient photocatalyst for the utilization of solar energy to decompose contaminants. To further improve the photocatalytic performance of such a Z-scheme BiOBr/g-C_3N_4 system, a high-efficiency direct Z-scheme type photocatalyst is proposed in which the photo-induced electrons can reduce unnecessary loss during transfer process by direct contact between BiOBr and g-C_3N_4. Furthermore, for the past few years, BiOBr has been synthesized *via* different methods, such as solvothermal, chemical precipitation, hydrothermal and so on. Among the different synthesis methods, a BiOBr microsphere structure obtained by a hydrothermal method reveals a remarkably photocatalytic activity thanks to its abundant porous structures providing BiOBr with sufficient active sites for the elimination of organic pollutants. To improve the microstructure on the basis of BiOBr microspheres, a facile template-assisted hydrothermal method was selected for the synthesis of BiOBr microspheres. Among the precursor solutions, ethylene glycol was used for prompting BiOBr nanosheets to self-assemble into microspheres. Simultaneously, the bio-template
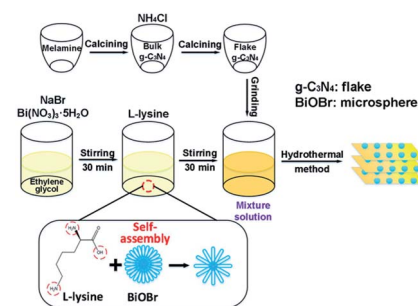

Fig. 1 Abridged summarization of the synthesis process of the BiOBr/g-C_3N_4 composites.

L-lysine with the polar functional groups of amino and hydroxyl, as a special surfactant, was used for regulating the microstructure of BiOBr microspheres so as to increase the efficacious active sites on the BiOBr surface.[25–27] To the best of our knowledge, only a few researchers have focused on direct Z-scheme BiOBr/g-C_3N_4 composites synthesized by a template-assisted hydrothermal method and the number of efficient direct Z-scheme photocatalysts is still finite.

In this study, a direct Z-scheme BiOBr microsphere/g-C_3N_4 flake heterojunction photocatalysts was successfully synthesized *via* a facile template-assisted hydrothermal method which enabled BiOBr microspheres to *in situ* grow on the surface of g-C_3N_4 flakes (Fig. 1). Through exploring the microstructure, optical and electrochemical properties of the composites, the BiOBr/g-C_3N_4 composites exhibit a higher photocatalytic activity proved by the degradation of RhB and TC-HCl, which could be attributed chiefly to the formation of a direct Z-scheme heterojunction system. Ultimately, a reasonable photocatalytic mechanism of the BiOBr/g-C_3N_4 composites for the degradation of RhB is contrastively analyzed and proposed by free radical trapping experiments.

2. Experimental

2.1. Chemicals

All the chemicals were used as received without further purification. Bismuth nitrate pentahydrate ($Bi(NO_3)_3 \cdot 5H_2O$) was acquired from Tianjin Kemiou Chemical Reagent Co. (Tianjing, China). Sodium bromide (NaBr) was acquired from Wuhan Tiantai Chemical Co. (Wuhan, China). Ethylene glycol (($CH_2OH)_2$), sodium hydroxide (NaOH), ethyl alcohol absolute (C_2H_6O) and ammonium chloride (NH_4Cl) were purchased from Tianjin Tianli Chemical Reagent Co. (Tianjing, China). Tetracycline hydrochloride (TC-HCl, $C_{22}H_{24}N_2O_8 \cdot HCl$) was purchased from Shanghai Macklin Biochemical Technology Co. (Shanghai, China).

2.2. Synthesis of g-C_3N_4 flakes

Fig. 1 illustrates the synthesis procedure of the BiOBr/g-C_3N_4 composites and the particular processes were as follows: 10 g melamine was sintered at 550 °C with a heating rate of 3 °C min^{-1} in a muffle furnace for 4 h. The bulk-g-C_3N_4 was obtained after cooling down to room temperature. After 4.5 g of

NH$_4$Cl particles were dissolved in 50 mL of deionized water, 6 g of the obtained bulk-g-C$_3$N$_4$ was added in solution under vigorous stirring and sonicated for 2 h. Thereafter, the suspension was dried at 80 °C in a drying oven overnight. Afterwards, the obtained dry g-C$_3$N$_4$ was sintered at 550 °C once again with a heating rate of 3 °C min^{-1} in a muffle furnace for 4 h. The flakes of g-C$_3$N$_4$ were obtained after cooling down to room temperature.

2.3. Synthesis of BiOBr/g-C$_3$N$_4$ nanocomposites

In a peculiar template-assisted hydrothermal process (Fig. 1), 0.16 mmol Bi(NO$_3$)$_3$·5H$_2$O and 0.16 mmol NaBr were dissolved into 50 mL of ethylene glycol solution and magnetically stirred for 30 min to form a clear solution. Then, 0.16 mmol L-lysine was dispersed into the above mixture solution and stirred for 30 min, followed by adding 0.95 g of as-prepared g-C$_3$N$_4$ flakes under vigorous stirring and sonicated for 2 h. Subsequently, the pH value of the mixture was adjusted to 5 by adding NaOH solution under constant stirring. After the suspension was transferred to a Teflon-lined stainless-steel autoclave and maintained at 120 °C for 12 h, the resultant suspension was respectively washed with deionized water and ethyl alcohol three times. The wet products were dried at 80 °C to obtain the BiOBr/g-C$_3$N$_4$ composite with a BiOBr mass ratio of 5%. BiOBr/g-C$_3$N$_4$ nanocomposites with different mass ratios of BiOBr (5%, 10%, 15%, 20% and 25%) were synthesized similarly by tuning the dosage of BiOBr. The corresponding BiOBr/g-C$_3$N$_4$ samples are abbreviated as B-5/CN, B-10/CN, B-15/CN, B-20/CN and B-25/CN. For comparison, pure BiOBr and g-C$_3$N$_4$ photocatalysts were prepared under the same conditions.

2.4. Characterization

The samples were characterized by X-ray diffraction (XRD) (D/max-2500, Rigaku), field emission scanning electron microscopy (FESEM) (Gemini SEM 300, Zeiss) and transmission electron microscope (TEM) (H-7650, Hitachi). Optical diffuse reflectance spectra (DRS) were measured by using UV-vis DRS (CARY 5000, Agilent).

The electrochemical impedance spectroscopy (EIS) and photocurrent (PC) responses measurements were performed by using an electrochemical workstation (CHI660E, CH Instruments Ins.) with a standard three-electrode configuration at room temperature. The as-prepared sample, a Pt wire and Ag/AgCl were used as the working electrode, counter electrode and reference electrode, respectively. The working electrode was prepared by a fluorinated tin oxide (FTO) sheet glass with an active area of 1 × 1 cm^2 containing 10 mg of photocatalyst and ultimately calcined at 105 °C for 2 h. The EIS experiment was executed in an aqueous 0.5 M Na$_2$SO$_4$ solution under dark conditions. For the PC measurement, a 500 W Xe lamp and Na$_2$SO$_4$ (0.5 M) aqueous solution served as the light source and electrolyte, respectively.

2.5. Photocatalytic activity

The photocatalytic activities of the as-prepared samples were evaluated by means of the degradation of the RhB solutions under a 500 W Xe-lamp with a cut off filter ($\lambda \geqq$ 420 nm). Briefly, the process was performed through immersing 50 mg of the as-prepared samples into 50 mL of RhB (TC-HCl) at an initial concentration of 15 mg L^{-1} (20 mg L^{-1}). Before lighting up the illuminant, the adsorption–desorption equilibrium was achieved by continuously stirring the suspensions in the dark for 40 min. At a certain time interval, 4 mL of the suspension was fetched and centrifuged to obtain a purified liquid. Finally, the RhB and TC-HCl concentrations were detected *via* the UV-vis spectrophotometer (UV-1200, Macy) at an absorption wavelength of 554 nm for RhB and 356 nm for TC-HCl. The stability of the B-20/CN composites was evaluated by four successive cycling experiments.

3. Results and discussion

3.1. Crystal structures of the samples

Fig. 2 exhibits XRD patterns of all the synthesized samples. Pure g-C$_3$N$_4$ shows distinct diffraction peaks at approximately 27.5°, corresponding to the (002) planes of g-C$_3$N$_4$ (JCPDS no. 87-1526). The diffraction peaks at $2\theta = 10.9°$, 25.2°, 32.2°, 40.6°, 46.2°, and 57.2° correspond to the (001), (101), (110), (112), (200), and (212) crystal planes of BiOBr (JCPDS No. 09-0393). Moreover, no other diffraction peaks were detected, revealing the high purity and single phase of the as-obtained samples. However, no other characteristic peaks of BiOBr were detected in B-5/CN except diffraction peaks at $2\theta = 25.2°$ and 32.2°, owing to the low BiOBr content in the B-5/CN composite. With the increase of BiOBr content, the characteristic peaks intensity of BiOBr also have increases of varying degree. Meanwhile, the characteristic peak intensities of g-C$_3$N$_4$ gradually weaken thanks to the decrease of g-C$_3$N$_4$ content. The strong diffraction peaks correspond with g-C$_3$N$_4$ and BiOBr, which indicates that the BiOBr/g-C$_3$N$_4$ composites were successfully synthesized through the facile template-assisted hydrothermal method.

3.2. Morphology characteristics of the samples

The microstructures and morphology of the as-prepared samples were observed by FESEM and TEM, and the results are displayed in Fig. 3. As can be seen from the FESEM image of pure g-C$_3$N$_4$ in Fig. 3a, the pure g-C$_3$N$_4$ synthesized by simple polymerization and gas phase methods consists of thin flakes
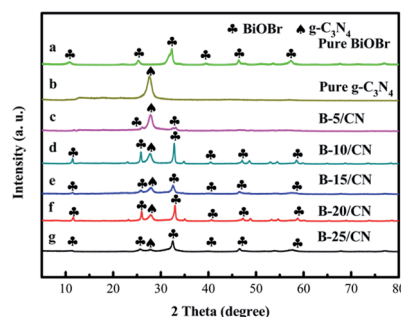

Fig. 2 XRD patterns of (a) pure BiOBr, (b) pure g-C$_3$N$_4$, (c) B-5/CN, (d) B-10/CN, (e) B-15/CN, (f) B-20/CN and (g) B-25/CN.

with an approximate thickness of 200 nm. The small thickness of g-C$_3$N$_4$ flakes is conducive to the separation of photo-generated carriers and the increase of built-in electric field intensity perpendicular to the lamellae.[28] From Fig. 3b, BiOBr microspheres are hardly detected on the surface of g-C$_3$N$_4$ flakes on account of the lower BiOBr content of the B-5/CN sample of than others. As you can see from Fig. 3c–f, BiOBr microspheres are randomly dispersed on the surface of the g-C$_3$N$_4$ flakes and between the g-C$_3$N$_4$ flakes. With the increase of BiOBr content, the number of BiOBr microspheres on the surface of the g-C$_3$N$_4$ flakes gradually multiplies. Furthermore, from the FESEM image of B-20/CN in Fig. 3e, a mass of BiOBr microspheres existed between the g-C$_3$N$_4$ flakes which provided multiple cellular structures for the BiOBr/g-C$_3$N$_4$ composites. Such structures are convincing evidence that the B-20/CN sample possesses a better photoabsorption performance than the other samples in below UV–vis DRS spectra.

A TEM image of B-20/CN is shown in Fig. 3g, providing a more distinct observation about the two components. The darker area with a spherical shape ought to be BiOBr and the lighter area should be g-C$_3$N$_4$, which further testifies the good dispersion of BiOBr microspheres on the g-C$_3$N$_4$ flakes and the direct contact between the two components. Homogeneous dispersion of the BiOBr microspheres constructs an effective physical junction between the BiOBr and g-C$_3$N$_4$ semi-conductors that unquestionably will accelerate the generation and separation of photo-generated carriers due to the direct Z-scheme heterojunction structure of the composites.[29,30] Furthermore, TEM images of template-free BiOBr and BiOBr prepared by using a bio-template are shown in Fig. 3h and i, reflecting the effect of a bio-template on the microsphere structures within the BiOBr photocatalyst. Obviously, BiOBr microspheres consist of vast BiOBr nanosheets *via* a self-assembly process. Meanwhile, the bio-template L-lysine[25–27] with polar functional groups of amino and hydroxyl, as a special surfactant, can selectively adsorb on specific crystal faces and control the crystal growth and self-assembly process of BiOBr. Compared with template-free BiOBr (Fig. 3h), the internal structure of BiOBr microspheres (diameter: about 400 nm) prepared by using the bio-template (Fig. 3i) shows more loose structures and a further exposure degree of the BiOBr nano-sheets in order to enhance the amount of active sites for the degradation of organic pollutants.

3.3. UV-vis DRS and band gap analysis

The optical properties of the as-prepared samples with different BiOBr content were evaluated by UV-vis DRS. From Fig. 4a, the
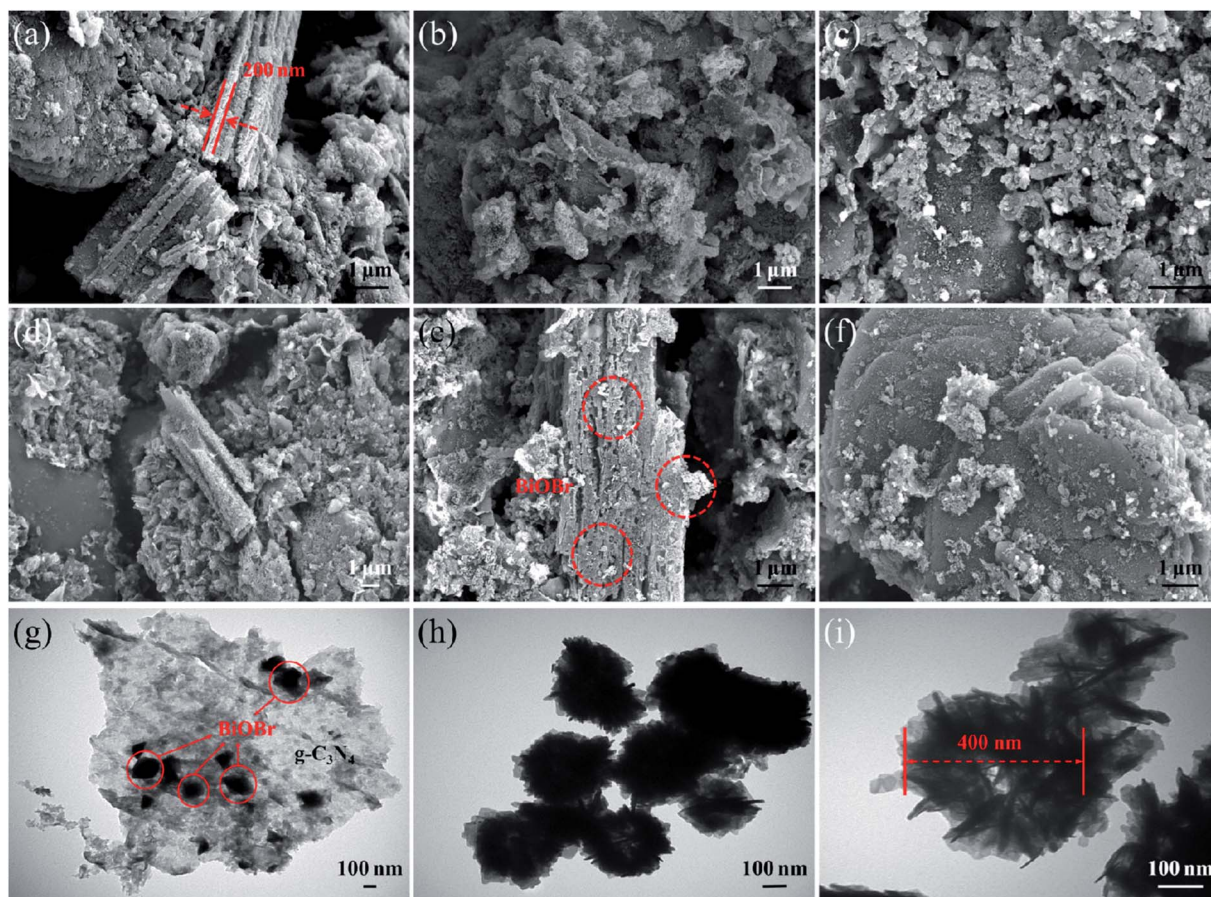

Fig. 3 FESEM images of (a) pure g-C$_3$N$_4$, (b) B-5/CN, (c) B-10/CN, (d) B-15/CN, (e) B-20/CN, (f) B-25/CN, TEM images of (g) B-20/CN, (h) template-free BiOBr and (i) BiOBr prepared by using bio-templates.

light absorption edges of g-C$_3$N$_4$ and BiOBr are approximately 465 and 428 nm, respectively. After g-C$_3$N$_4$ combines with BiOBr, the light absorption edge of the B-5/CN composite has red-shifted to 470 nm, which indicates that the BiOBr microspheres are likely to settle onto the surface of g-C$_3$N$_4$ flakes. It's worth noting that the photoabsorption performance of the blended samples seems stronger than those of pure g-C$_3$N$_4$ and BiOBr in the range of 470–495 nm. This phenomenon can be ascribed to the irregular cellular structure of BiOBr microspheres scattering and reflecting light, as well as the strong interfacial interaction between BiOBr and g-C$_3$N$_4$ in the BiOBr/g-C$_3$N$_4$ hetero-phase junction.[31]

Fine approximations of the band gaps of BiOBr and g-C$_3$N$_4$ semiconductors are provided in Fig. 4b. From the spectra, the band gaps (E_g) of g-C$_3$N$_4$ and BiOBr are 2.50 and 3.05 eV, respectively. Furthermore, the conduction band (CB) and valence band (VB) edge redox potentials of g-C$_3$N$_4$ and BiOBr can be estimated on the basis of the extensively accepted equations:

$$E_{CB} = X - E_e - E_g/2 \tag{1}$$

$$E_{VB} = E_{CB} + E_g \tag{2}$$

The X values for BiOBr and g-C$_3$N$_4$ are 6.18 eV and 4.73 eV, respectively.[32,33] E_{VB} and E_{CB} stand for the VB and CB potentials, respectively, and E_e is the energy of free electrons on the hydrogen scale (about 4.5 eV).[34] According to eqn (1) and (2), the E_{CB} and E_{VB} of g-C$_3$N$_4$ are −1.02 and +1.48 eV, respectively. Furthermore, the E_{CB} and E_{VB} of BiOBr are +0.16 and +3.21 eV, respectively.

3.4. EIS analysis and photocurrent response measurements

EIS analysis and photocurrent response measurements were applied to testify the high efficiency of direct Z-scheme BiOBr/g-C$_3$N$_4$ hybrids in facilitating the segregation of photogenerated electron–hole pairs. The EIS spectra of pure BiOBr, pure g-C$_3$N$_4$ and the B-20/CN composite are shown in Fig. 4c. The diameter of the EIS Nyquist plot of B-20/CN is smaller than those of pure BiOBr and g-C$_3$N$_4$. Given that the diameters on the EIS spectra reveal the reaction rate at the surface of the electrode, the plots in Fig. 4c display that B-20/CN possesses a lower resistance than pure BiOBr and g-C$_3$N$_4$. It's worth noting that lower resistance is conducive to accelerating the interfacial charge transfer and separating photo-generated electron–hole pairs.[35] Fig. 4d reveals the photoelectric conversion ability for pure g-C$_3$N$_4$, pure BiOBr and the B-20/CN electrodes. As is well-known, during the electron transfer from the CB of samples to the electrodes, the photocurrent is simultaneously generated. Generally speaking, the sample with a higher photocurrent signifies the presence of a longer lifetime of the photo-generated electrons and holes which enhances the photocatalytic activity.[36] As is shown in Fig. 4d, high-frequency and consistent photocurrent responses are visibly observed for each switch-on and switch-off event in the electrodes. The photocurrent of the B-20/CN electrode is higher than those of the pure g-C$_3$N$_4$ and BiOBr electrodes. This conclusion is in accordance with the EIS analyses, and explicitly indicates that the introduction of BiOBr into g-C$_3$N$_4$ can effectively promote the separation of photogenerated electron–hole pairs.

3.5. Photocatalytic activity

The photocatalytic activity of all the semiconductor photocatalysts was measured by degrading RhB under visible light irradiation. Before irradiation, the adsorption–desorption equilibrium between the RhB solution and photocatalyst was attained by magnetic stirring for 40 min under dark conditions. From Fig. 5a, it can be observed that the direct photolysis of RhB is negligible without the addition of a photocatalyst. Pure g-C$_3$N$_4$ possesses a relatively lower photocatalyst activity than those of the other BiOBr/g-C$_3$N$_4$ composites, and only 53.2% of RhB was degraded within 120 min. In addition, the pure BiOBr has a relatively higher adsorptive property and photocatalyst activity than those of pure g-C$_3$N$_4$ due to the special structure of the microspheres, and 59.9% of RhB was degraded within 120 min. With an incremental BiOBr content, the photocatalytic efficiency of the composites was gradually improved due to the formation of direct Z-scheme heterostructures and the resulting promotion of light absorption properties in the visible light range.[37] The B-20/CN composite with an optimal photocatalytic efficiency can decompose 97.1% of RhB. Nonetheless, while the mass ratio of BiOBr was higher than 20%, the photocatalytic efficiency of B-25/CN decreased by 11.5% for the degradation of RhB. This phenomenon can be attributed to the excessive BiOBr covering the active sites of g-C$_3$N$_4$, leading to a low photocatalytic performance.

Moreover, aiming to intensively research the kinetics curves of the photodegradation of RhB, the experimental data were applied to a pseudo-first-order model:
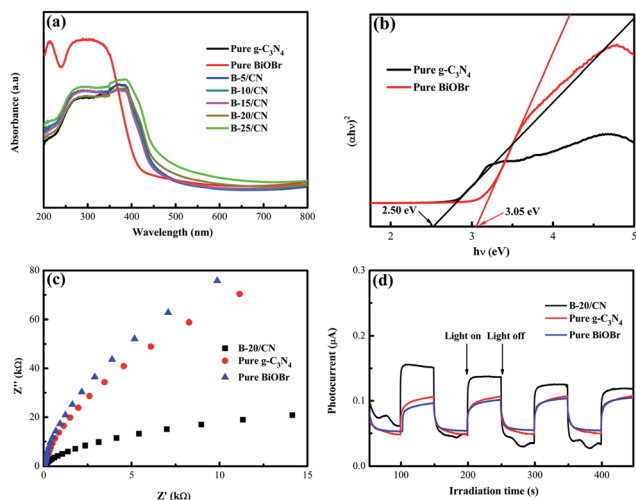
$$\ln\left(\frac{C_0}{C_t}\right) = kt \tag{3}$$

Fig. 4 (a) DRS spectra; (b) plot of $(\alpha h\nu)^2$ vs. $h\nu$; (c) EIS Nyquist plot and (d) transient photocurrent response of the as-prepared samples with light on/off cycles.
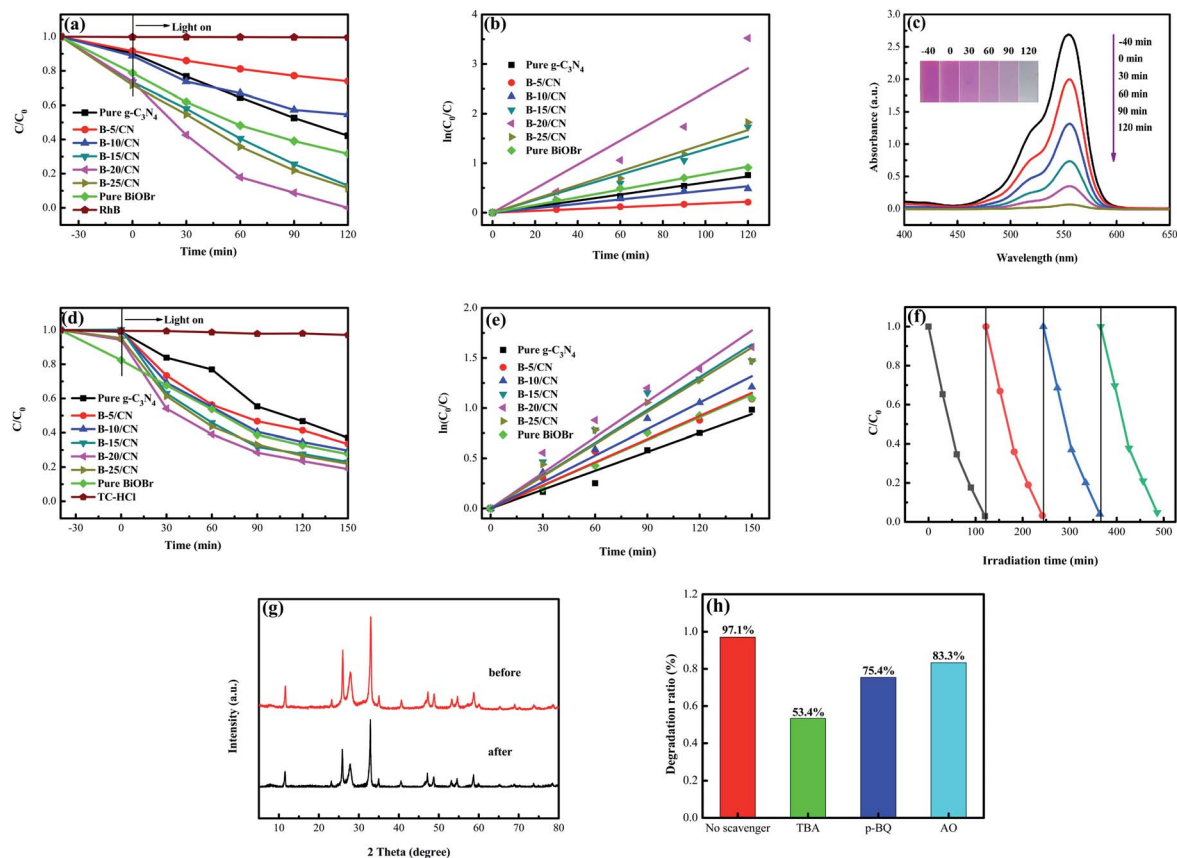
Fig. 5 (a) Photocatalytic activity for the degradation of RhB; (b) the relative pseudo-first-order kinetic plots; (c) UV-vis spectral curves of RhB degradation over B-20/CN; (d) photocatalytic activity for the degradation of TC-HCl; (e) the relative pseudo-first-order kinetic plots of the as-prepared samples; (f) four recycling runs of B-20/CN for the degradation of RhB; (g) the XRD patterns of B-20/CN samples before and after the photocatalytic degradation experiments for RhB and (h) the effects of various scavengers on the degradation efficiency of B-20/CN toward RhB.

where C_0 and C_t are the concentrations of the RhB solution at times 0 and t, respectively, and k is the pseudo-first-order rate constant (min^{-1}). From Fig. 5b and Table 1, the degradation of B-20/CN is 0.02427 min^{-1}, which is 3.97 and 3.14 times higher than those for pure g-C$_3$N$_4$ and BiOBr, respectively. The result further illustrates that BiOBr coupled with g-C$_3$N$_4$ can enhance the transfer and separation efficiency of photo-generated carriers, and thus increase the photocatalytic activity.[38] Fig. 5c displays the evolution of the absorption spectra of the RhB

solution over B-20/CN every 30 min. As can be seen from the spectra, the absorption peak intensity of the RhB solution gradually reduces with the extension of irradiation time and tends to be gentle after 120 min. The corresponding solution color gradually fades away.

To shield against specific degradation of the photocatalysts, TC-HCl, regarded as an antibiotic residue, was applied to evaluate the photocatalytic efficiency of the as-prepared samples under visible light irradiation.[39] From Fig. 5d, it can be observed that the direct photolysis of TC-HCl is negligible without the photocatalysts. Not surprisingly, the B-20/CN sample exhibits the highest photodegradation efficiency for TC-HCl, which can reach 81.1% within 150 min. With the increasing BiOBr content, the photocatalytic efficiency of the composites was gradually promoted compared with pure g-C$_3$N$_4$ and BiOBr. However, for the BiOBr content higher than 20%, a further augmentation of the BiOBr content leads to a decrease in the photocatalytic efficiency of TC-HCl degradation. The photodegradation process of TC-HCl accords with a pseudo-first order model (Fig. 5e). The degradation rate of B-20/CN is 1.87, 1.57, 1.53, 1.39, 1.08 and 1.11 times higher than those for pure g-C$_3$N$_4$, pure BiOBr, B-5/CN, B-10/CN, B-15/CN and B-25/CN, respectively (Table 1). The above conclusion testifies that the

Table 1 The kinetics of the degradation reaction under visible light irradiation

Samples	Degradation rate (Vis)	
	RhB (min^{-1})	TC-HCl (min^{-1})
Pure g-C$_3$N$_4$	0.0061	0.0063
Pure BiOBr	0.0077	0.0075
B-5/CN	0.0018	0.0077
B-10/CN	0.0044	0.0088
B-15/CN	0.0128	0.0109
B-20/CN	0.0242	0.0118
B-25/CN	0.0139	0.0106

B-20/CN composite possesses a great potential to decompose antibiotics from the sewage of the pharmaceuticals industry.

As shown in Fig. 5f, in order to evaluate the stability of the as-prepared photocatalyst, B-20/CN was selected for a recycling test to degrade RhB under visible light irradiation. After four recycling runs, the degradation efficiency diminished from 97.1% to 95.3%, indicating that the B-20/CN composite exhibits an excellent photocatalysis stability. Furthermore, to further testify the stability of the B-20/CN photocatalyst, the XRD pattern after the photocatalytic degradation experiments for RhB was measured.[35] The result (Fig. 5g) exhibits that the crystal structure did not change during the photocatalytic degradation of RhB. Hence, the B-20/CN composite has a remarkable stability and recyclability.
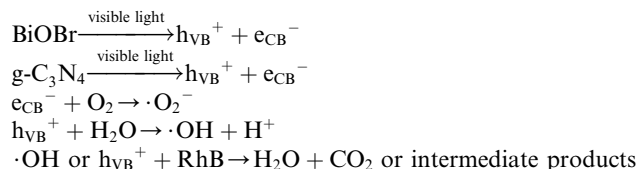
To illustrate the photocatalytic mechanism of the B-20/CN photocatalyst, the primary active groups generated in the photodegradation process were detected *via* an active-groups-trapping experiment. In this experiment, tertiary butanol (TBA), benzoquinone (*p*-BQ) and ammonium oxalate (AO) served as the scavengers for $\cdot OH$, $\cdot O_2^-$ and h^+, respectively.[40] Fig. 5h demonstrates the effects of the three scavengers on the photodegradation process of RhB. As TBA, *p*-BQ and AO were added into the photocatalytic process, the photocatalytic degradation efficiency of B-20/CN was reduced from 97.1% to 53.4%, 75.4% and 83.3%, respectively. The results indicate that the $\cdot OH$, $\cdot O_2^-$ and h^+ play major roles in the degradation course of RhB.

3.6. Photocatalytic mechanism

According to the free radical trapping experiments, as well as optical and electrochemical analysis, a possible photocatalytic mechanism of BiOBr/g-C$_3$N$_4$ photocatalyst is elaborated in Fig. 6. Followed by BiOBr and g-C$_3$N$_4$ being stimulated under visible light irradiation, photoexcited electrons (e^-) and holes (h^+) are located in their VB and CB, respectively. For BiOBr/g-C$_3$N$_4$, the transfer process of the photo-generated of e^- and h^+ can be classified as a type II heterojunction structure (Fig. 6a).[41] Chiefly, the VB potential of g-C$_3$N$_4$ (+1.48 eV) is more negative than that of BiOBr (+3.21 eV) and the CB potential of g-C$_3$N$_4$ (−1.02 eV) is more negative than that of BiOBr (+0.16 eV).[42] Secondly, since the band gap of g-C$_3$N$_4$ (E_g = 2.50 eV) is narrower than that of BiOBr (E_g = 3.05 eV), the VB of g-C$_3$N$_4$ is likely to generate more carriers than BiOBr under visible light irradiation.[43] For the above two reasons, the e^- from the CB of g-

C$_3$N$_4$ can transmit to the CB of BiOBr and the h^+ from VB of BiOBr can simultaneously transfer to the VB of g-C$_3$N$_4$. As a result, the e^- and h^+ may respectively concentrate on the CB of BiOBr and the VB of g-C$_3$N$_4$, which effectually restrains the recombination of e^- and h^+. Nevertheless, during the migration of e^-/h^+ to more positive/negative energy levels, the reducing capacity of the photo-generated electrons and oxidizing capacity of the photo-generated holes will be subject to inevitable loss.[44]

Obviously, in the direct Z-scheme BiOBr/g-C$_3$N$_4$ heterojunction structure (Fig. 6b), the contact surface between BiOBr and g-C$_3$N$_4$ serves as a charge transmission bridge to facilitate annihilation of electron–hole pairs with a weaker oxidation–reduction ability, which efficiently figures out the above deficiency.[45,46] According to energy band theory, the photo-generated e^- in the CB of BiOBr can quickly transfer to the contact surface through the Schottky barrier[47,48] and recombine with h^+ on the VB of g-C$_3$N$_4$, leaving the e^-/h^+ with a stronger oxidation-reduction ability in the CB/VB of g-C$_3$N$_4$/BiOBr. Moreover, the CB potential of g-C$_3$N$_4$ is more negative than $E^0(O_2/\cdot O_2^-)$, which means the e^- on the CB of g-C$_3$N$_4$ can more easily reduce O_2 to $\cdot O_2^-$.[49,50] Meantime, the VB potential of BiOBr is more positive than $E^0(H_2O/\cdot OH)$, so the h^+ in the VB of BiOBr is capable of oxidizing H_2O to $\cdot OH$. The active groups, such as $\cdot O_2^-$ and $\cdot OH$, are able to directly react with RhB to produce CO_2, H_2O or intermediate products.[51,52] The procedure can be depicted as follows:

$$BiOBr \xrightarrow{\text{visible light}} h_{VB}^+ + e_{CB}^-$$
$$g\text{-}C_3N_4 \xrightarrow{\text{visible light}} h_{VB}^+ + e_{CB}^-$$
$$e_{CB}^- + O_2 \rightarrow \cdot O_2^-$$
$$h_{VB}^+ + H_2O \rightarrow \cdot OH + H^+$$
$$\cdot OH \text{ or } h_{VB}^+ + RhB \rightarrow H_2O + CO_2 \text{ or intermediate products}$$

The deduction is well in accord with the above conclusion of the radical trapping experiments that the $\cdot O_2^-$, $\cdot OH$ and h^+ are the primary oxidation active groups for the degradation of RhB.

4. Conclusions

In summary, a direct Z-scheme BiOBr/g-C$_3$N$_4$ heterojunction system has been successfully constructed *via* a facile template-assisted hydrothermal method. Compared with pure g-C$_3$N$_4$ and BiOBr, the BiOBr/g-C$_3$N$_4$ composite with a BiOBr mass ratio of 20% (B-20/CN) exhibits a more remarkable photocatalytic performance for the degradation of RhB and TC-HCl. In such a direct Z-scheme system, the intimate synergistic interactions between BiOBr and g-C$_3$N$_4$, the significant extension of the light absorption edge, as well as the segregation of the strong oxidation–reduction capacity of e^- and h^+ lead to the remarkable photocatalytic activity of BiOBr/g-C$_3$N$_4$ composites. The trapping experiments manifest that the $\cdot OH$, $\cdot O_2^-$ and h^+ are the main active groups for the degradation of RhB. Moreover, the as-prepared B-20/CN composite exhibits excellent photostability and reusability after 4 runs under the same conditions. This work is supposed to open up new insights into the structural design of novel direct Z-scheme photocatalysts with a high
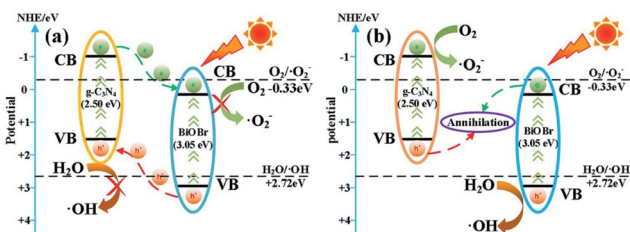

Fig. 6 Schematic of charge carriers transfer in (a) BiOBr/g-C$_3$N$_4$ heterojunction and (b) direct Z-scheme BiOBr/g-C$_3$N$_4$ heterojunction.

photoactivity and further employment in the fields of the environment and energy.

Conflicts of interest

The authors declare that there are no conflicts of interest.

Acknowledgements

References

1 Z. Y. Ruan, G. H. Liu, J. X. Shu, C. G. Ren and Z. H. Wang, *RSC Adv.*, 2019, **9**, 5858–5864.

2 S. D. Balgude, Y. A. Sethi, B. B. Kale, D. P. Amalnerkar and P. V. Adhyapak, *RSC Adv.*, 2019, **9**, 10289–10296.

3 M. Sabet, S. Saeednia, M. Hatefi-Ardakani and R. Sheykhisarem, *Nano-Struct. Nano-Objects*, 2018, **13**, 21–29.

4 N. Tian, H. W. Huang, Y. He, Y. X. Guo, T. R. Zhang and Y. H. Zhang, *Dalton Trans.*, 2015, **44**, 4297–4307.

5 L. Cheng, Q. J. Xiang, Y. L. Liao and H. W. Zhang, *Energy Environ. Sci.*, 2018, **11**, 1362–1391.

6 X. Li, J. G. Yu and M. Jaroniec, *Chem. Soc. Rev.*, 2016, **45**, 2603–2636.

7 Z. F. Huang, L. Pan, J. J. Zou, X. W. Zhang and L. Wang, *Nanoscale*, 2014, **6**, 14044–14063.

8 L. L. Zhang, H. C. Zhang, H. Huang, Y. Liu and Z. H. Kang, *New J. Chem.*, 2012, **36**, 1541–1544.

9 C. Wang, X. M. Wang, B. Q. Xu, J. C. Zhao, B. X. Mai, P. A. Peng, G. Y. Sheng and J. M. Fu, *J. Photochem. Photobiol., A*, 2004, **168**, 47–52.

10 D. W. Jing and L. J. Guo, *J. Phys. Chem. B*, 2006, **110**, 11139–11145.

11 M. C. Long, W. M. Cai, J. Cai, B. X. Zhou, X. Y. Chai and Y. H. Wu, *J. Phys. Chem. B*, 2006, **110**, 20211–20216.

12 A. Petala, D. Spyrou, Z. Frontistis, D. Mantzavinos and D. I. Kondarides, *Catal. Today*, 2019, **328**, 223–229.

13 Y. Zhang, J. Di, W. Tong, X. L. Chen, J. Z. Zhao, P. H. Ding, S. Yin, J. X. Xia and H. M. Li, *Res. Chem. Intermed.*, 2019, **45**, 437–451.

14 F. Cao, J. M. Wang, Y. N. Wang, J. Zhou, S. Li, G. W. Qin and W. Q. Fan, *Nanoscale Adv.*, 2019, **1**, 1124–1129.

15 D. L. Huang, Z. H. Li, G. M. Zeng, C. Y. Zhou, W. J. Xue, X. M. Gong, X. L. Yan, S. Chen, W. J. Wang and M. Cheng, *Appl. Catal., B*, 2019, **240**, 153–173.

16 S. Zhang, P. C. Gu, R. Ma, C. T. Luo, T. Wen, G. X. Zhao, W. C. Cheng and X. K. Wang, *Catal. Today*, 2019, **335**, 65–77.

17 R. G. He, K. Y. Cheng, Z. Y. Wei, S. Y. Zhang and D. F. Xu, *Appl. Surf. Sci.*, 2019, **465**, 964–972.

18 Z. F. Jiang, W. M. Wan, H. M. Li, S. Q. Yuan, H. J. Zhao and P. K. Wong, *Adv. Mater.*, 2018, **30**, 1706108.

19 A. Mishra, A. Mehta, S. Basu, S. Shetti and P. Nagaraj, *Carbon*, 2019, **149**, 693–721.

20 M. J. Lima, A. M. T. Silva, C. G. Silva and J. L. Faria, *J. Catal.*, 2017, **353**, 44–53.

21 A. Iwase, Y. H. Ng, Y. Ishiguro, A. Kudo and R. Amal, *J. Am. Chem. Soc.*, 2011, **133**, 11054–11057.

22 J. Fu, Y. L. Tian, B. B. Chang, F. N. Xi and X. P. Dong, *J. Mater. Res.*, 2012, **22**, 21159–21166.

23 L. D. Cao, D. K. Ma, Z. L. Zhou, C. L. Xu, C. Cao, P. Y. Zhao and Q. L. Huang, *Chem. Eng. J.*, 2019, **368**, 212–222.

24 M. M. Zhang, C. Lai, B. S. Li, D. L. Huang, G. M. Zeng, P. Xu, L. Qin, S. Y. Liu, X. G. Liu, H. Yi, M. F. Li, C. C. Chu and Z. Chen, *J. Catal.*, 2019, **369**, 469–481.

25 P. Alam, P. Fagerlund, P. Hägerstrand, J. Töyrylä, S. Amini, M. Tadayon, A. Miserez, V. Kumar, M. Pahlevan and M. Toivakka, *Compos. Appl. Sci. Manuf.*, 2015, **75**, 84–88.

26 J. Zhang, J. H. Hu, D. T. Wu, J. F. Ma, Y. X. Tao, Y. Qin and Y. Kong, *Int. J. Biol. Macromol.*, 2019, **129**, 786–791.

27 D. G. He, X. X. He, K. M. Wang and Y. X. Zhao, *Chin. Chem. Lett.*, 2013, **24**, 99–102.

28 J. Li, Y. Yu and L. Z. Zhang, *Nanoscale*, 2014, **6**, 8473–8488.

29 J. J. Liu, B. Cheng and J. G. Yu, *Phys. Chem. Chem. Phys.*, 2016, **18**, 31175–31183.

30 Y. Z. Hong, Y. H. Jiang, C. S. Li, W. Q. Fan, X. Yan, M. Yan and W. D. Shi, *Appl. Catal., B*, 2016, **180**, 663–673.

31 M. S. Zhu, S. Y. Kim, L. Mao, M. Fujitsuka, J. Y. Zhang, X. C. Wang and T. Majima, *J. Am. Chem. Soc.*, 2017, **139**, 13234–13242.

32 Y. X. Chen, X. B. Ji, S. Vadivel and B. Paul, *Ceram. Int.*, 2018, **44**, 23320–23323.

33 J. F. Zhang, J. W. Fu, Z. L. Wang, B. Cheng, K. Dai and W. K. Ho, *J. Alloys Compd.*, 2018, **766**, 841–850.

34 Y. Bai, P. Q. Wang, J. Y. Liu and X. J. Liu, *RSC Adv.*, 2014, **4**, 19456–19461.

35 Z. J. Xie, Y. P. Feng, F. L. Wang, D. N. Chen, Q. X. Zhang, Y. Q. Zeng, W. Y. Lv and G. G. Liu, *Appl. Catal., B*, 2018, **229**, 96–104.

36 Y. M. He, L. H. Zhang, M. H. Fan, X. X. Wang, M. L. Walbridge, Q. Y. Nong, Y. Wu and L. H. Zhao, *Sol. Energy Mater. Sol. Cells*, 2015, **137**, 175–184.

37 X. B. Chen, S. H. Shen, L. J. Guo and S. S. Mao, *Chem. Rev.*, 2010, **110**, 6503–6570.

38 A. Houas, H. Lachheb, M. Ksibi, E. Elaloui, C. Guillard and J. M. Herrmann, *Appl. Catal., B*, 2001, **31**, 145–157.

39 Q. Yang, Z. Chen, X. R. Yang, D. T. Zhou, X. X. Qian, J. J. Zhang and D. Zhang, *Mater. Lett.*, 2018, **212**, 41–44.

40 R. G. He, J. Q. Zhou, H. Q. Fu, S. Y. Zhang and C. J. Jiang, *Appl. Surf. Sci.*, 2018, **430**, 273–282.

41 J. X. Low, J. G. Yu, M. Jaroniec, S. Wageh and A. A. Al-Ghamdi, *Adv. Mater.*, 2017, **29**, 1601694.

42 R. Dingle, H. L. Störmer, A. C. Gossard and W. Wiegmann, *Appl. Phys. Lett.*, 1978, **33**, 665–667.

43 F. L. Liu, C. Huang, C. X. Liu, R. Shi and Y. Chen, *Chem.–Eur. J.*, 2019, DOI: 10.1002/chem.201904594.

44 X. Q. Liu and L. Cai, *Appl. Surf. Sci.*, 2018, **445**, 242–254.

45 J. Yang, H. T. Zhang, B. B. Chen, H. Tang, C. S. Li and Z. Z. Zhang, *RSC Adv.*, 2015, **5**, 64254–64260.

46 J. G. Yu, S. H. Wang, J. X. Low and W. Xiao, *Phys. Chem. Chem. Phys.*, 2013, **15**, 16883–16890.

47 T. T. Jiang, J. L. Li, Y. Gao, L. Li, T. Lu and L. K. Pan, *J. Colloid Interface Sci.*, 2017, **490**, 812–818.

48 J. F. Zhang, Y. F. Hu, X. L. Jiang, S. F. Chen, S. G. Meng and X. L. Fu, *J. Hazard. Mater.*, 2014, **280**, 713–722.

49 P. F. Xia, B. C. Zhu, B. Cheng, J. G. Yu and J. S. Xu, *ACS Sustain. Chem. Eng.*, 2017, **6**, 965–973.

50 W. K. Jo and T. S. Natarajan, *Chem. Eng. J.*, 2015, **281**, 549–565.

51 Q. L. Xu, L. Y. Zhang, J. G. Yu, S. Wageh, A. A. Al-Ghamdi and M. Jaroniec, *Mater. Today*, 2018, **21**, 1042–1063.

52 H. J. Li, W. G. Tu, Y. Zhou and Z. G. Zou, *Adv. Sci.*, 2016, **3**, 1500389.